

# Progress in characterization of the pedestal structure, stability and fluctuations during ELM cycle on NSTX

A. Diallo<sup>1</sup>, J. Canik<sup>2</sup>, G.J. Kramer<sup>1</sup>, S-H. Ku<sup>1</sup>, J. Manickam<sup>1</sup>, R. Maingi<sup>2</sup>, D. Smith<sup>4</sup>, P. Snyder<sup>5</sup>, T. Osborne<sup>5</sup>, R.E. Bell<sup>1</sup>, C-S. Chang<sup>1</sup>, W. Guttenfelder<sup>1</sup>, B.P. LeBlanc<sup>1</sup> and S. Sabbagh<sup>6</sup>

<sup>1</sup>Princeton Plasma Physics Laboratory, Princeton University, Princeton, NJ, USA

<sup>2</sup>Oak Ridge National Laboratory, Oak Ridge, TN, USA

<sup>3</sup>University of California, Los Angeles, CA, USA

<sup>4</sup>University of Wisconsin, Madison, WI, USA

<sup>5</sup>General Atomics, San Diego, CA, USA

<sup>6</sup>Columbia University, New York, NY, USA

*Corresponding author:* adiallo@pppl.gov

## Abstract:

The edge stability and pedestal structure are important for achieving high performance pedestals necessary for maximum core fusion gain in future next-step devices. The stability of the pedestal is characterized in high performance discharges in National Spherical Torus Experiment (NSTX). In addition, the spatial structure of turbulence present during an ELM cycle in the pedestal region indicates spatial scales  $k_{\perp}\rho_i^{\text{ped}}$  ranging from 0.2 to 0.7 propagating in the ion diamagnetic drift direction at the pedestal top. These propagating spatial scales are found to be poloidally elongated and consistent with ion-scale microturbulence. Nonlinear gyrokinetic simulations – XGC1 – find localized fluctuations agreeing with experimental level radial and poloidal correlation lengths.

## 1 Introduction

Performance projections for the International Thermonuclear Experimental Reactor (ITER) [1] have emphasized the relation between fusion gain of the burning plasma core and the edge pedestal in the high confinement (H-mode) regime. Using multiple transport models, the fusion performance for ITER has been predicted to be proportional to the pedestal temperature height squared at fixed density (effectively proportional to the pressure pedestal height). [2] Due to this strong dependence, the pedestal height emerges as a control knob for fusion performance. However, increasing the pedestal height is limited by a class of instabilities known as edge localized modes (ELM). [3] The peeling ballooning theory [3] is the leading candidate in explaining the process that limits the increase of the pedestal height. This theory constitutes the backbone of the recently developed predictive model EPED. [4] The main hypothesis of this model is that the pedestal pressure height is

limited by the peeling ballooning instability, and the pressure gradient is limited by kinetic ballooning modes (KBMs).

This model has successfully predicted the pedestal height and width in several standard aspect ratio ( $R/a \sim 3$ ) tokamak experiments. [4] In low aspect ratio tokamaks such as National Spherical Torus Experiment (NSTX) [5], however, the applicability of the EPED model is not yet established, but elements of the EPED hypothesis are being tested separately (e.g., stability and fluctuations).

This paper focuses on the edge stability analysis for high performance discharges on NSTX. In addition, we characterize the spatial scales during the inter-ELM phase in the pedestal region and perform comparison with gyrokinetic codes XGC1. Finally, a discussion and summary are presented on the theoretical implications of the microturbulence in the pedestal region and possible links to the pedestal structure evolution.

## 2 Experimental Method

NSTX [5] is a medium-sized low aspect-ratio spherical torus (ST) with major radius  $R \sim 0.85$  m, minor radius  $a \leq 0.67$  m, and  $B_\phi \leq 0.55$  T. H-mode discharges are typically obtained using neutral beam injection (NBI) heating with powers up to 6 MW. The discharges studied used a marginally double-null divertor configuration, with the plasma slightly biased down ( $\delta_r^{sep} \sim -5$  mm, where  $\delta_r^{sep}$  represents the radial distance between the upper and lower X-points mapped to the outer midplane), and a bottom triangularity  $\delta_{bot} \sim 0.6$ . The upper triangularity was typically kept at 0.4 while the elongation  $\kappa$  varied between 2.3 and 2.4.

The dataset shown was obtained from discharges at constant  $B_\phi = 0.45$  T, and NBI power of 6 MW, with amounts of lithium evaporated less than 50 mg between discharges

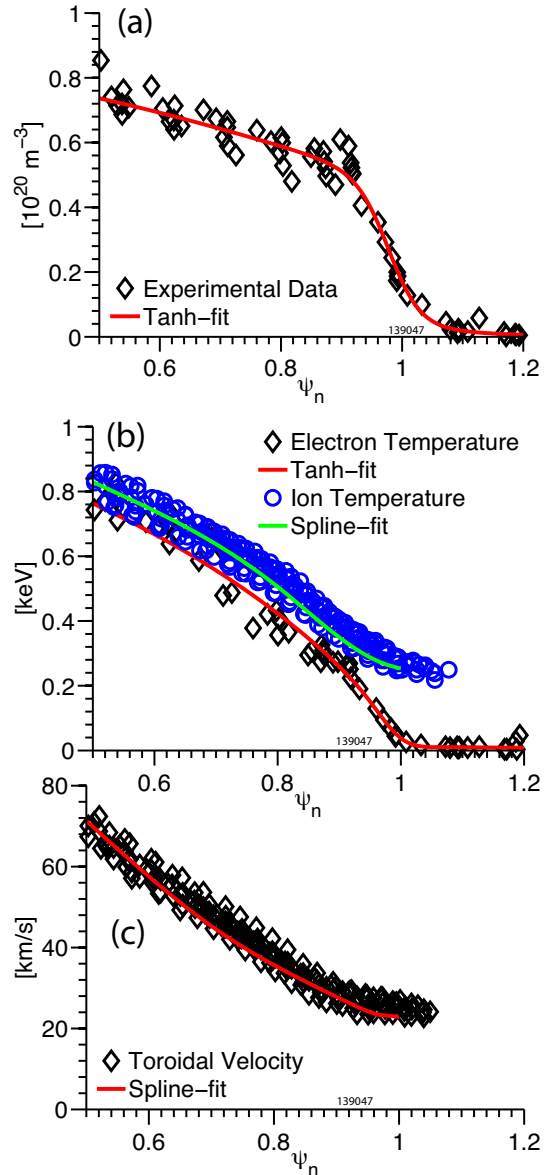


FIG. 1: Experimental radial profiles: (a) electron density with overlaid tanh-fit; (b) Both ion and electron temperatures with overlaid fits. Note that ion profile is spline fitted. (c) Toroidal velocity.

to ensure reproducible ELMs. Large amounts of evaporated lithium ( $> 200$  mg) enables access to ELM-free regimes. [6] Figure 1 displays the electron density, ion and electron temperatures, and the toroidal velocity during the last 50% of the ELM cycle. In addition, the associated profile fits are shown (the details of the profile fitting technique are given in Ref. [7].)

### 3 Edge stability calculations

In recent previous work, we analyzed the inter-ELM evolution of the pressure pedestal parameters and showed that the pressure pedestal height saturates during approximately the last 30% of the ELM cycle in low and medium plasma current [8]. In this section, we analyze the edge stability prior to the onset of ELM.

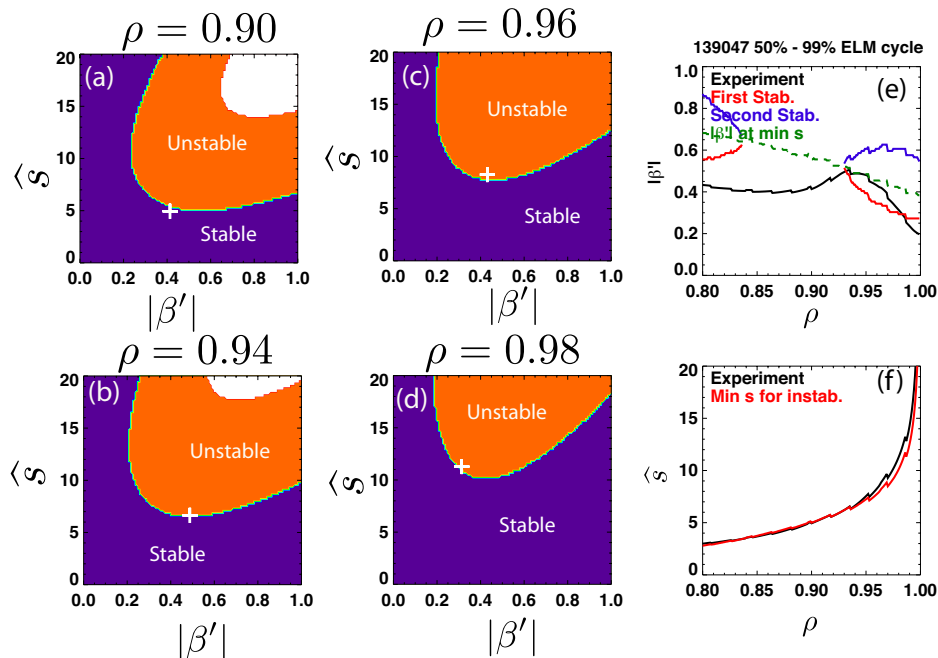


FIG. 2: “Ball” calculations for 50% - 99% of the ELM cycle. (a)-(d) Ideal  $n = \infty$  MHD stability diagram  $\hat{s} - |\beta'|$  for various radii. The white crosses indicate the experimental shears and pressure gradients. (e) Experimental  $\beta'$  showing that the pedestal ( $\rho = 0.93 - 0.98$ ) crosses the first stability boundary and is therefore ballooning unstable.

An infinite- $n$  ideal ballooning stability code (BALL a module of GS2) is used to determine the pedestal stability (see also Canik et al. [9]). Figures 2(a)-(d) display  $\hat{s} - |\beta'|$  stability diagrams at various radii in the pedestal region during the last part of the ELM cycle (50% - 99%). Here  $\beta'$  is proportional to the pressure gradient and the white crosses indicate the experimental shears and pressure gradients. Here, the experimental magnetic shear —  $\hat{s} = r/q\partial q/\partial r$ — is determined from an edge reconstruction that includes the bootstrap current (computed using the Sauter model). Figure 2(e) displays the first and second stabilities and clearly shows that the pedestal top ( $\rho = 0.93 - 0.98$ ) is ballooning unstable.

Using a set of fixed boundary kinetic equilibrium fits (EFITs) during the last part of

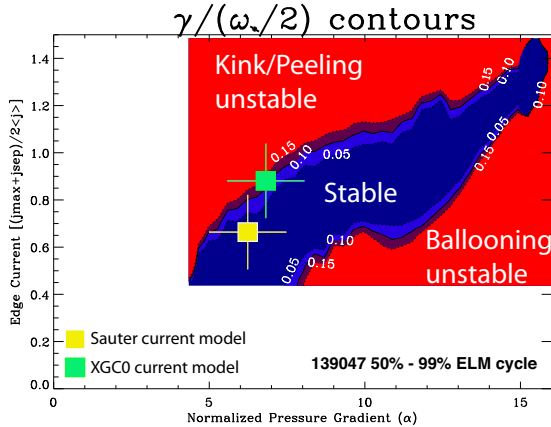


FIG. 3: *ELITE* Peeling-ballooning mode stability diagram. Contours of growth rate over  $1/2$  ion diamagnetic frequency ( $\omega_i^*$ ) as a function of normalized pressure gradient and normalized current density.

ELM cycle, while varying the edge pressure gradient at fixed edge current and vice versa, the stability of each equilibrium is computed using the *ELITE* MHD stability code [10] for  $n=3, 6, 9, 12, 15$ . Figure 3 displays such equilibria-generated-boundaries with the cross-hairs representing the experimental current density and pressure gradient. Here, we display cross-hairs using the Sauter and XGC0 [22] current models. As shown, XGC0 calculations of the bootstrap current is 20 -30% larger than that of the Sauter model, which put the experimental point closer to the current driven kink/peeling stability boundary. PEST calculations of this discharge equilibrium indicate instability at low- $n$  ( $n = 2, 3, 4$ ) kink/peeling, with the maximum linear growth rate at  $n=3$ .

This stability analysis is consistent with previous work where the pedestal height saturates during approximately the last 30% of the ELM cycle for both low and medium plasma current. It can be concluded that this limit in the pedestal height is reached when the peak pedestal pressure gradient and computed edge current of the equilibrium are near the kink/peeling ballooning boundary. These results extend previous analysis of ELMy discharges at lower injected power [11, 23] to high performance discharges.

## 4 Pedestal structure scalings

While the peeling-ballooning theory sets an upper limit on the pedestal height, the width is hypothesized—by the leading pedestal height prediction model (EPED)—to be set by the kinetic ballooning modes (KBM) [12]. During its onset, KBM is thought to be responsible for large transport in all channels (momentum, particle and heat for both electrons and ions). Such transport could contribute to limiting the pedestal width. The pedestal width is shown to scale with  $(\beta_{pol}^{ped})^{1/2}$  ( $\beta_{pol}^{ped} = 2\mu_0 P_{ped}/B_\theta^2$ ;  $P_{ped}$  is the pedestal

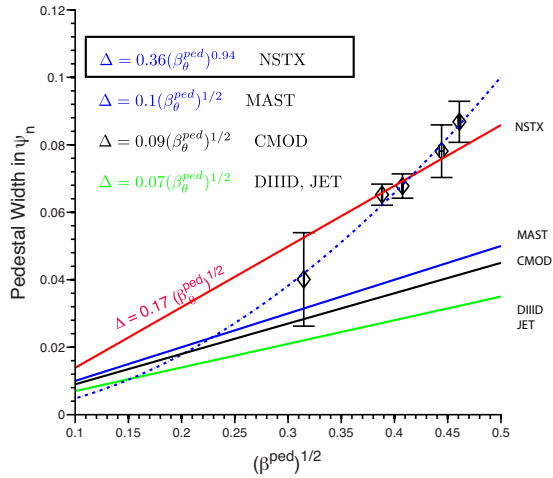


FIG. 4: The pedestal width (in  $\psi_n$ ) scaling with  $(\beta_{pol}^{ped})^{1/2}$ . This width scaling effectively provides a relation between the width and the height of the pedestal. The best fit for NSTX width is  $(\beta_{pol}^{ped})^{0.94}$  as displayed with the dotted curve.

height,  $B_\theta$  represents the poloidal field) and has been reported in multiple tokamaks (see Figure 4). This  $-(\beta_{\text{pol}}^{\text{ped}})^{1/2}$  - scaling is expected if the pressure gradient is limited by KBM. [12] Relaxing, however, the linear scaling in  $(\beta_{\text{pol}}^{\text{ped}})^{1/2}$  shows that NSTX data can also be fitted with  $(\beta_{\text{pol}}^{\text{ped}})^{0.94}$  as displayed in figure 4. This near  $\beta_{\text{pol}}^{\text{ped}}$  scaling is predicted if ETG modes are the dominant players in the pedestals [21]. This differences in exponent is not yet understood. It is important to note that the observed width in NSTX is 2.4 larger than DIII-D and C-Mod, and 1.7 times wider than MAST. Can differences in scaling point to competing mechanisms for setting the pedestal width? Experimental identification of KBM instabilities is challenging because it requires high spatial and temporal resolution of the local turbulence in the pedestal. However, there is growing evidence of the existence of KBM and microtearing modes in both MAST and NSTX pedestal regions using gyrokinetic simulations [13, 14].

## 5 Spatial characterization of the edge fluctuations

In this section, we focus on characterizing the spatial scales of the fluctuations in the pedestal between ELMs. We utilize correlation reflectometry [16] and beam emission spectroscopy (BES) diagnostic systems [17]. These two diagnostics enable the determination of the radial and poloidal spatial structure of fluctuations in the pedestal region, together with propagation in the poloidal direction.

Characterization of the edge density fluctuations in the radial direction is facilitated by an array of fixed-frequency quadrature reflectometers allowing for excellent coverage of the pedestal region of high performance plasmas in NSTX. Figure 5 displays the evolution between ELMs of the radial correlation length of the complex electric field associated with the density fluctuations at the density pedestal top and in the steep gradient region. In this figure, the radial correlation length is observed to increase at the pedestal top by a factor of 2. During the last 50% of ELM cycle, the radial correlation reaches  $7\rho_i^{\text{ped}}$ . In the steep gradient, however, the correlation remains unchanged through the ELM cycle. An increase in the radial correlation length could suggest an enhancement of the radial transport at the pedestal top assuming these correlation lengths are proxy for the eddy sizes.

Figure 6 displays both the inter-ELM group velocities determined from the time lags between BES channels. BES signals were frequency filtered to isolate 8-50 kHz components, the typical frequency range for observed broadband turbulence [18]. On the right panel of figure 6, the  $E_r \times B$  velocity is displayed at the pedestal top. This velocity is inferred from the force-balance equation of the carbon ion distribution from the CHERS

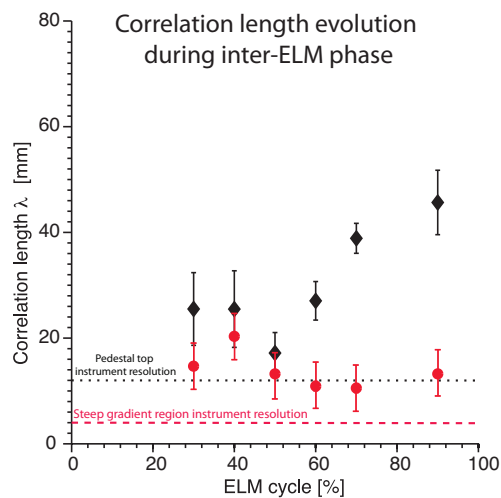


FIG. 5: Evolution of the radial correlation length in the pedestal regions: pedestal top (diamond) and steep gradient (circle).

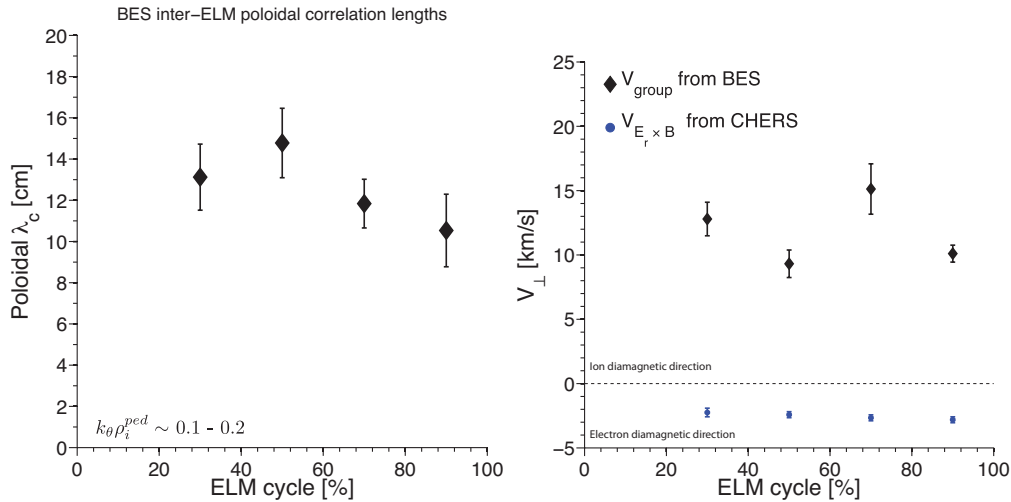


FIG. 6: Inter-ELM poloidal correlation length evolution measured using the BES system. Poloidal velocity evolution. The diamond symbols represent the group velocities determined using BES. The circle symbols indicate the  $E_r \times B$  velocities obtained from the CHERS system at the pedestal top ( $R \sim 1.40$  m). Note that positive velocity represents propagation in the ion diamagnetic direction while negative velocity indicates a propagation in the electron diamagnetic direction.

system. The BES velocities represent the advection velocities of the eddies. In order to relate these velocities with the propagation velocities, we account for the  $E_r \times B$  velocities at the pedestal top ( $R \sim 1.40$  m). It is clear from figure 6 that the  $E_r \times B$  velocities are measurably smaller at the pedestal top than BES-determined group velocities, and in the opposite direction. This is contrary to observations in the DIII-D tokamaks where both group velocities and  $E_r \times B$  velocities are large and in the same direction. [19] The propagation velocities, determined from  $v_{E_r \times B}^{CHERS} + v_{group}^{BES}$ , clearly show propagation in the ion diamagnetic direction and are consistent with propagation velocities inferred from figure 5 of Yan *et al.* [19] Note that positive velocity represents propagation in the ion diamagnetic direction while negative velocity indicates a propagation in the electron diamagnetic direction (see figure 6). Differences observed between the absolute individual values of  $v_{E_r \times B}^{CHERS}$  and  $v_{group}^{BES}$  between the DIII-D and NSTX are not yet well understood. The edge density fluctuations in the pedestal region during the ELM cycle clearly show anisotropic fluctuations and spatial scales indicative of ion-scale turbulence propagating in the ion diamagnetic direction. Given these measurements of the pedestal turbulence during the inter-ELM phase, it is clear that the fluctuations exhibit ion-scale microturbulence compatible with ITG (including hybrids TEM) and/or KBM instabilities.

## 6 Comparison with XGC1 simulations

To gain some physical insights in the spatial characterization of the fluctuations observed in pedestal region from the BES system, we used the global gyrokinetic edge code XGC1 [20] to study the ITG turbulence. Usefulness of a localized gyrokinetic simulation

is highly limited in the edge pedestal since the radial correlation length is similar to or longer than the radial pedestal width. Realistic experimental profiles of 139047 are used, but Coulomb collisions were not turned on in order to study the collisionless physics first. For a clearer analysis under given experimental plasma profiles, XGC1 was operated in the  $\delta$ -f mode, even though XGC1 normally operates in full-f mode in predictive simulations. 10 million particles are used for this simulation. The simulation box extends from central core up to  $\psi_n = 0.95$ . Figure 7 displays a cross-section of the potential fluctuations in the non-linear stage of the simulation, which shows characteristic poloidal structures propagating in the ion diamagnetic direction. ITG source is found to reside at the pedestal top, but nonlinearly and nonlocally penetrated into the pedestal region. Sampling a region encompassing both BES and the reflectometer measurements (as indicated in the second panel of FIG 7), one can estimate the equivalent radial and poloidal correlations as shown in the third panel of FIG 7. The correlation is obtained from band-pass filtered potential fluctuations consistent with the BES frequency window. A good agreement is obtained. Poloidal correlation length of approximately 11 cm is obtained from simulation, compared to 10 to 14 cm from BES. Radial correlation length of approximately 4 cm is obtained from simulation, compared to 2 to 4 cm from correlation reflectometry. Future simulations will include possible modifications by the Coulomb collisions, by the addition of kinetic electrons and by multiscale interaction with background neoclassical flows.

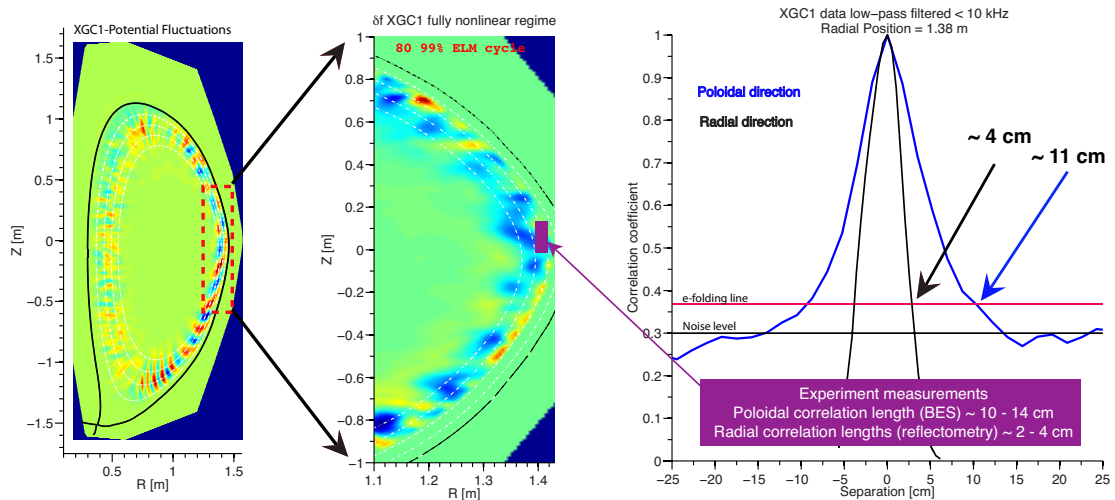


FIG. 7: Left panel: 2D cross-section of the potential fluctuations from XGC1 simulations in the fully nonlinear stage. Middle panel: Zoomed in edge fluctuations indicating the BES and reflectometry measurements region. Right panel: Evaluations (from simulation) of both radial (4 cm) and poloidal correlation (11 cm) lengths in the edge region showing experimental level radial and poloidal correlation lengths.

## 7 Summary

We have extended studies of the pedestal structure during the inter-ELM phase to include stability analysis and further the understanding of the limiting mechanisms during

the pedestal height dynamics. This latter part was addressed through the characterization of the fluctuation spatial scales at play during the inter-ELM evolution.

Specifically, detailed measurements of the fluctuations spatial structure in the pedestal top and steep gradient regions during the ELM cycle are reported. Using diagnostics that probe density fluctuations in both poloidal and radial directions, spatial scales at the pedestal top are observed and found consistent with ion-scale microturbulence propagating in the ion diamagnetic directions.

Two theoretical candidates consistent with the measured ion scale turbulence are the ITG/TEM and KBM instabilities. Initial verifications were performed using the gyrokinetic code XGC1. Using experimental profiles, the simulations show, in a fully nonlinear stage, that both radial and poloidal correlations agree with the experimentally measured correlation lengths. These simulations are being extended to include electron dynamics and electromagnetic effects.

While only ion scale fluctuations are observed, electron scale dynamics are not being ruled out. In fact, typical microinstability parameters such as  $R/L_{Te}$  is overall 60% larger than  $R/L_{Ti}$  and 6 times greater than  $R/L_{ne}$ . This points to potential electron scale dynamics capable of impacting the pedestal width scaling: this is addressed in [21].

A.D. acknowledges discussions with N. Crocker. This work is supported by U.S. Dept of Energy contracts DE-AC02-09CH11466.

## References

- [1] ITER Physics Basis Editors, Nucl. Fusion **39** (1999) 2137.
- [2] KINSEY, J. et al., Nuclear Fusion **51** (2011) 083001.
- [3] CONNOR, J. W. et al., Phys. of Plasmas **5** (1998) 2687.
- [4] SNYDER, P. et al., Nuclear Fusion **51** (2011) 103016.
- [5] ONO, M. et al., Nuclear Fusion **40** (2000) 557.
- [6] BELL, M. G. et al., Plasma Physics and Controlled Fusion **51** (2009) 124054.
- [7] OSBORNE, T. H. et al., Journal of Phys.: Conf. Series **123** (2008) 012014.
- [8] DIALLO, A. et al., Nuclear Fusion **51** (2011) 103031.
- [9] CANIK, J. M. et al., 536-EX/P7-16 – this conference.
- [10] SNYDER, P. B. et al., Phys. of Plasmas **9** (2002) 2037.
- [11] MAINGI, R. et al., Phys. Rev. Lett. **103** (2009) 075001.
- [12] SNYDER, P. B. et al., Phys. Plasmas **16** (2009) 056118.
- [13] DICKINSON, D. et al., Phys. Rev. Lett. **108** (2012) 135002.
- [14] GUTTENFELDER, W. et al., Physics of Plasmas **19** (2012) 056119.
- [15] YAN, Z. et al., Physics of Plasmas **18** (2011) 056117.
- [16] CROCKER, N. A. et al., Plasma Physics and Controlled Fusion **53** (2011) 105001.
- [17] SMITH, D. R. et al., Review of Scientific Instruments **81** (2010) 10D717.
- [18] SMITH, D. R. et al., EX/P7-18 – this conference.
- [19] YAN, Z. et al., Phys. Rev. Lett. **107** (2011) 055004.
- [20] KU, S-H. et al., Nuclear Fusion **49** (2009) 115021.
- [21] KAW, P. K. et al., 618-TH/P4-15 – this conference.
- [22] CHANG, C-S, et al., 597-TH/P4-12 – this conference.
- [23] BOYLE, D. P. et al., Plasma Physics and Controlled Fusion **53** (2011) 105011.